Journal of Crystal Growth 601 (2023) 126911

Contents lists available at ScienceDirect

Journal of Crystal Growth

journal homepage: www.elsevier.com/locate/jcrysgro

Onion-Like nanoparticles of the metal–organic framework UiO-66 synthesized by sequential spike crystal growth

Adam F. Cahn [a,1], Rebecca L. Combs [a], Ellen M. Monzo [a], Steven D. Prinslow [a], Celina M. Harris [a], R. Lee Penn [a,*]

[a] Department of Chemistry, University of Minnesota Twin Cities, 207 Pleasant Street SE, Minneapolis, MN 55455, United States

ARTICLE INFO

Communicated by: James J. De Yoreo

Keywords:
A1 Characterization
A1 Crystal Morphology
A1 X-ray Diffraction
A2 Seed Crystals
B1 Metal–Organic Frameworks
B1 Nanomaterials

ABSTRACT

Reproducible size and morphology of metal–organic framework (MOF) particles are essential for tuning these materials for applications like heterogeneous catalysis. Particle size measurements from electron micrographs provide information about the impact of changing synthetic parameters on MOF growth, but reported data are usually limited to averages and statistical distributions. Further elucidating synthetic control parameters could facilitate studies of facet-dependent and non-classical growth mechanisms. In this work, phase-pure nanoparticles of the MOF UiO-66 were synthesized using alternating spikes of zirconium and hafnium-based nodes, forming an onion-like structure with alternating layers of Zr-UiO-66 and Hf-UiO-66. In conventional, bright-field transmission electron micrographs, Hf-UiO-66 and Zr-UiO-66 layers appeared darker and lighter, respectively. Alternating layers of Hf-UiO-66 and Zr-UiO-66 were also apparent in elemental maps obtained using scanning transmission electron microscopy with energy-dispersive X-ray spectroscopy. Average particle sizes increased monotonically with each spike, and no Zr-only or Hf-only particles were observed after the first spike, indicating that new material was consistently incorporated onto existing seeds. Surface area of the onion-like particles and their uptake of Ni^{2+} from solution were both between the values measured for Zr-UiO-66 and Hf-UiO-66. Results demonstrate the use of sequential spikes of nodes in monitoring crystal growth in MOFs.

1. Introduction

Metal–organic frameworks (MOFs) are a widely studied family of porous crystalline materials comprising inorganic nodes, which are typically metal ions or metal-oxide or metal-hydroxide clusters, coordinated to organic linkers. The extensive variety of available metal-linker combinations gives rise to a diversity of structures with applications that include heterogeneous catalysis, [1] gas storage and separation, [2] chemical sensing, [3] electronics, [4] and drug delivery [5]. To obtain homogeneous samples fine-tuned for specific applications, reproducible control over MOF physical properties and reactivities is necessary [6]. Methods for tuning particle size, [7] phase purity, [8] porosity, [9] catalytic function, [10] and other properties have been studied at length. Further understanding of MOF growth mechanisms and reactive sites is critical to designing experiments investigating these important parameters [11].

Nucleation and crystal growth of MOFs have been studied using *in situ* microscopy [12,13] X-ray diffraction, [14] and other techniques [15–17]. However, the complex and uncommon setups required for *in situ* instrumentation make them challenging to use in routine experiments. Results from *ex situ* post-synthetic characterization are common in the MOF literature, especially for determining particle size [18] and morphology [19] by transmission and scanning electron microscopies (TEM and SEM, respectively) and powder X-ray diffraction (XRD). Particle size measurements from TEM and SEM images are useful for quantifying growth but are usually limited to average size distributions over numerous particles, although the amount of material characterized is but a tiny amount (typically a fraction of a picogram even over hundreds of particle size measurements). Phase identification and particle size measurements using XRD amount to weighted averages. Additionally, multimodal size distributions and mixtures of morphologies and phases often complicate the study of crystal growth using methods based on microscopy and scattering. A further confounding factor is that crystal growth typically occurs by multiple mechanisms, [20] which

* Corresponding author.
E-mail address: rleepenn@umn.edu (R. Lee Penn).
[1] Present address: Department of Chemistry, University of California Berkeley, Berkeley, California 94720, United States.

https://doi.org/10.1016/j.jcrysgro.2022.126911
Received 15 July 2022; Received in revised form 27 September 2022; Accepted 7 October 2022
Available online 13 October 2022

may include non-classical crystal growth mechanisms like oriented attachment [21]. A more detailed understanding of such processes is aided by the sub-nanometer length scale characterization of nanoparticles collected at different stages of crystal growth.

The archetypal MOF UiO-66 is constructed from $Zr_6(\mu_3\text{-}O)_4(\mu_3\text{-}OH)_4$ nodes that are each coordinated to 12 benzene-1,4-dicarboxylate (BDC) linkers in a face-centered cubic structure (Fig. 1). Like other zirconium-based MOFs, UiO-66 generally exhibits high thermal and chemical stability [22,23]. Hafnium and zirconium-based UiO-66 are isostructural [24] and have similar physical and chemical properties, but the higher oxophilicity of Hf (Hf–O and Zr–O bond dissociation energies, BDEs, are 801 and 766 kJ mol^{-1}, respectively) makes Hf-UiO-66 more Brønsted acidic and resistant to decomposition than Zr-UiO-66 [25,26]. Acid modulators are commonly used to synthesize crystalline UiO-66 with controlled particle size, [27] and the product materials can then be modified to tune reactivity for specific applications. Examples of these modifications include installation of metal cations or complexes [28] onto the metal nodes and organic functionalization of the BDC linker [29].

Hierarchical MOF-on-MOF structures with enhanced adsorptive and luminescent properties, as compared to their constituent MOFs, have been reported with UiO-66 cores [30] and shells, [31] respectively. These hybrid materials are prepared by injecting seed crystals of one MOF (the core) into a reaction vessel containing precursor components of another MOF, which can result in the growth of a shell of the new material around the original seeds [30,31]. Promoting heterogrowth onto the seed crystals typically requires close structural compatibility (*e.g.*, similar lattice parameters or spacings between metal nodes at specific crystallographic faces) between the core and shell MOFs [32]. Structural compatibility can be achieved by varying the metal cation [33,34] or the linker [35] with each spike of precursor, such that the core and shell MOFs are isostructural. For example, particles with a Zr-UiO-67 core and Hf-UiO-67 shell (UiO-67 is a linker-expanded analogue of UiO-66) have been synthesized by Luo *et al.* [36].

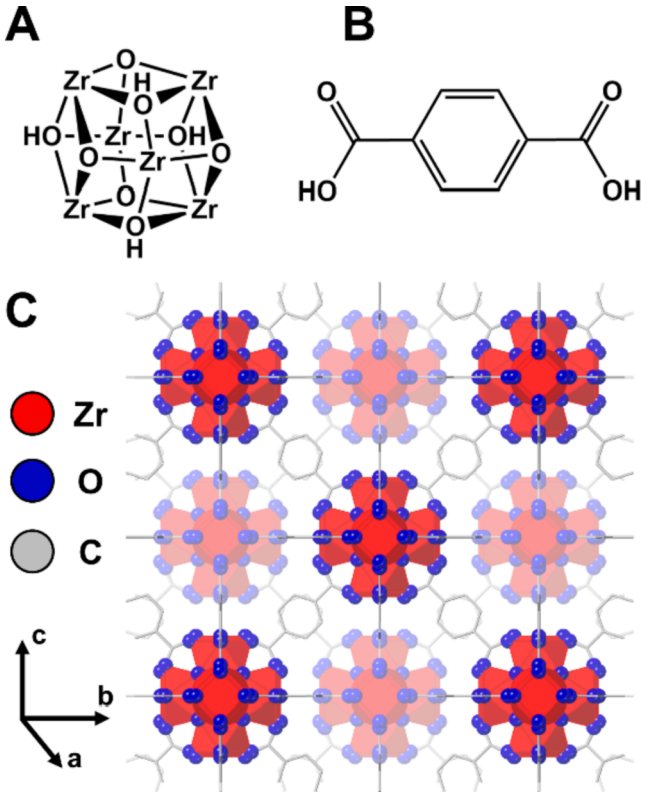

Fig. 1. Structure of UiO-66 showing an octahedral Zr_6 node (A), benzene-1,4-dicarboxylic acid linker (B), and polyhedral representation of the crystal structure (C). Hydrogen atoms in (C) are omitted for clarity.

In this work, we used a similar seed-mediated sequential spike growth strategy to synthesize onion-like UiO-66 nanoparticles with alternating layers of Zr-based and Hf-based nodes, denoted as Zr-Hf-Zr-Hf-UiO-66. Product crystals consistently contain a distinct Zr-UiO-66 core and three layers of Hf-UiO-66 or Zr-UiO-66, with boundaries between Hf and Zr-rich regions that are clearly resolvable *via* conventional TEM and scanning TEM with energy-dispersive X-ray spectroscopy (STEM-EDS). Post-synthesis, nanoparticles were subjected to a simple solution-based deposition procedure to install Ni^{2+} cations onto the MOF, which enabled the evaluation of the accessibility of the metal nodes from a catalysis perspective. STEM-EDS results demonstrate that Ni^{2+} is present at modestly higher Ni^{2+}:node ratios in the core as compared to the outer layers. The sequential spike crystal growth technique provides a straightforward marker of the location and extent of crystal growth in UiO-66 and can be applied to other MOFs.

2. Experimental

2.1. Materials and methods

Zirconium(IV) chloride, 99.5 % ($ZrCl_4$, Sigma-Aldrich); hafnium(IV) chloride, 98 % ($HfCl_4$, Sigma-Aldrich); benzoic acid, 99.5 % (BA, Sigma-Aldrich); terephthalic acid, 98 % (BDC, Sigma-Aldrich); *N*,*N*-dimethylformamide, 99.8 % (DMF, Fisher); acetone, 99.5 % (Fisher); nickel (II) acetate tetrahydrate, 99 % ($Ni(OAc)_2{\cdot}4H_2O$, Acros Organics); methanol, 99.8 % (Sigma-Aldrich); dimethyl sulfoxide-d_6, 99.9 % (DMSO-d_6, Cambridge Isotope); sulfuric acid-d_2, 96–98 % (D_2SO_4, Sigma-Aldrich); nitric acid, 70 % (HNO_3, Sigma-Aldrich); hydrochloric acid, 36.5–38 % (HCl, VWR Analytical); and sulfuric acid, 95–98 % (H_2SO_4, Sigma-Aldrich) were used without further purification. All water used was purified using a Milli-Q Advantage A10 water purification system and had a resistivity of 18.2 MΩ·cm.

All reactions were performed without stirring in 20 mL scintillation vials in an aluminum heating block on a hot plate equipped with an IKA ETS-D5 programmable temperature probe. Ultrasonication was performed using a Branson 3800 Ultrasonic Cleaner. Centrifugation was performed using an Eppendorf Centrifuge 5804 with an FA-45–6-30 rotor.

2.2. Synthesis of Zr-Hf-UiO-66

Zr-Hf-UiO-66 was synthesized using a benzoic acid-modulated solvothermal procedure adapted from Schaate *et al.* [37] To prepare a Zr node solution, $ZrCl_4$ (20 mg, 0.0858 mmol) and BA (628.8 mg, 5.15 mmol) were suspended by ultrasonication in 8 mL DMF and heated at 100 °C for 1 h. A solution of BDC (14.3 mg, 0.0861 mmol) in 2 mL DMF was added, and the reaction mixture was heated at 100 °C for 48 h. The white Zr-UiO-66 product was isolated by centrifugation for 5 min at 10,000 rpm (13,776 rcf) and washed three times with 5 mL DMF. To prepare for a spike, the entire product was resuspended in 4.5 mL DMF. Meanwhile, a Hf node solution was prepared identically to the Zr node solution but with $HfCl_4$ (27.5 mg, 0.0859 mmol) instead of $ZrCl_4$ in 4.5 mL DMF. The suspension of Zr-UiO-66 and a solution of BDC (14.3 mg, 0.0861 mmol) in 1 mL DMF were added to the Hf node solution, and the reaction mixture was heated at 100 °C for 48 h. The final Zr-Hf-UiO-66 product was washed three times with 5 mL DMF and three times with 5 mL acetone before drying under ambient conditions. Yield: 26.9 mg (49 %).

2.3. Synthesis of Zr-Hf-Zr-Hf-UiO-66

Zr-Hf-Zr-Hf-UiO-66 was synthesized as above but with one additional spike each of the Zr and Hf node solutions. Yield: 80.8 mg (75 %).

2.4. Synthesis of Zr-UiO-66 and Hf-UiO-66

Zr-UiO-66 and Hf-UiO-66 were synthesized following the procedure for Zr-Hf-Zr-Hf-UiO-66 but with repeated spikes of only Zr or Hf node solutions, respectively. Yields: 108.5 mg (115 %) and 91.6 mg (74 %) for Zr-UiO-66 and Hf-UiO-66, respectively.

2.5. Ni loading

The solvothermal deposition of Ni^{2+} into product materials was adapted from the procedure described by Wang *et al.*, who reported the loading of Ni^{2+} into NU-1000, a MOF containing the same Zr_6 nodes as UiO-66 [38]. UiO-66 particles (~10 mg) were suspended by ultrasonication in a solution of $Ni(OAc)_2{\cdot}4H_2O$ (5 mg, 0.02 mmol) in 10 mL methanol and heated at 60 °C for 18 h. The white Ni@UiO-66 product was washed three times with 5 mL methanol and three times with 5 mL acetone before drying under ambient conditions. This procedure was performed with Zr-UiO-66, Hf-UiO-66, Zr-Hf-UiO-66, and Zr-Hf-Zr-Hf-UiO-66.

2.6. Characterization

XRD was performed on a PANalytical X'Pert Pro MPD diffractometer equipped with an X'Celerator detector in Bragg-Brentano geometry. All measurements were taken using Co Kα radiation (λ = 1.79 Å) at an accelerating voltage of 45 kV and an emission current of 40 mA. A 2θ range of 5–70° and a dwell time of 50 s were used.

N_2 isotherms were collected using a Quantachrome Autosorb iQ, and multi-point Brunauer-Emmett-Teller (BET) surface areas were calculated using the ASiQWin software using relative pressure (P/P_0) ranges of 0.05–0.20 (Zr-UiO-66 and Zr-Hf-Zr-Hf-UiO-66) and 0.05–0.25 (Hf-UiO-66). Isotherms were collected at 77 K after activating ~ 40 mg of sample for 24 h at 60 °C at atmospheric pressure and degassing under vacuum for 12 h at 150 °C.

TEM was performed using an FEI Tecnai T12 TEM with a LaB_6 filament, operated at an accelerating voltage of 120 kV. Particle sizes are reported as upper estimates, as measured by a straight line across the largest dimension of the particle in TEM images using ImageJ software (Figure S1).

STEM imaging and STEM-EDS were performed using an FEI Titan G2 field emission S/TEM or a Thermo Fisher TALOS F200X field emission S/TEM, both operated at an accelerating voltage of 200 kV. High-angle annular dark field (HAADF) images were collected using the E. A. Fischione Model 3000 annular detector. EDS spectra were obtained using the Super-X G1 EDS system and ESPRIT software on the Titan and using the Super-X G2 EDS system and Velox software on the TALOS. Quantitation of EDS spectra was performed using the Kα lines for Zr, Ni, and O and the Lα line for Hf.

Proton nuclear magnetic resonance (^{1}H NMR) spectroscopy was performed using a Bruker Avance III HD 400 MHz NMR spectrometer. To prepare a sample, UiO-66 (2–5 mg) was digested in 1 mL DMSO-d_6 with 3 drops of D_2SO_4 at 70 °C for 30 min. After cooling to room temperature, the optically clear solution was transferred to an NMR tube for analysis.

Inductively coupled plasma-optical emission spectroscopy (ICP-OES) was performed using a Thermo Scientific iCAP 7400 ICP-OES in radial mode using argon as a carrier gas. Peak areas were recorded in quadruplicate at 327.305, 277.336, and 221.647 nm for Zr, Hf, and Ni respectively. To prepare a sample, UiO-66 (2 mg) was digested in 1 mL concentrated HCl with 2 drops of concentrated H_2SO_4 at 70 °C for 30 min. After cooling to room temperature, 100 μL of the optically clear solution was diluted with 9 mL of water, and 1 mL of this solution was diluted with 10 mL of 1 % HNO_3. To construct calibration curves, 5 standards containing 0.05–2.5 ppm Zr, Hf, and Ni were prepared by serial dilution of aqueous stock solutions of $ZrCl_4$, $HfCl_4$, and $Ni(OAc)_2{\cdot}4H_2O$ (2000 ppm in each metal) in 0.015 M HCl/0.105 M HNO_3 to match the acid background from sample digestion.

3. Results and discussion

Sequential spike crystal growth, in which the Zr and Hf-based nodes were alternated, resulted in the formation of onion-like Zr-Hf-UiO-66 and Zr-Hf-Zr-Hf-UiO-66 particles. Powder XRD patterns of Zr-UiO-66, Hf-UiO-66, Zr-Hf-Zr-Hf-UiO-66 (Fig. 2A) and Zr-Hf-UiO-66 (Figure S3) demonstrate high crystallinity and phase purity, with no evidence for impurity phases detected. The agreement in d-spacings and relative peak heights among samples supports that Zr-UiO-66 and Hf-UiO-66 are isostructural and that the crystal structure does not change detectably with each sequential spike. Reflections at 14° 2θ in the synthesized materials are due to residual solvent molecules in the pores of the framework [39].

All samples exhibit type I N_2 sorption isotherms (Fig. 2B), characteristic of microporous UiO-66. The sharp increases in the volume of adsorbed gas near $P/P_0 = 1$, which are often observed with nanocrystalline materials, may be due to interparticle voids [40]. The BET surface area of 1163 m^2/g for Zr-UiO-66 is comparable to calculated and reported values [39]. The BET surface area of 885 m^2/g for Hf-UiO-66 agrees well with the predicted value of 888 m^2/g, which was calculated by dividing the Zr-UiO-66 surface area by 1.31 (Hf-UiO-66 is 31 % denser than Zr-UiO-66). Computing an average of the measured surface areas of Zr-UiO-66 and Hf-UiO-66 weighted by their densities yields a theoretical surface area of 1005 m^2/g for Zr-Hf-Zr-Hf-UiO-66, which is near the measured value of 1117 m^2/g. The observation that the experimental surface area is somewhat higher than the predicted one is consistent with the Zr:Hf molar ratio of 1.3 in the material, as determined using EDS and ICP-OES methods (see below).

Pore size distributions (Figure S5) show the presence of 5.5 and 11.5 Å pores, which have been described for UiO-66 in which 4 of the possible 12 linkers per node are missing. However, the BET surface areas were lower than what has previously been reported for Zr-UiO-66 with such defects (~1500 m^2/g) [41]. Incomplete activation of the materials before sorption measurements could lead to residual solvent in the pores and decreased surface areas. The discrepancy between experimental and literature values may also be a consequence of the BET method itself, which is known to produce considerably different surface areas for the same sample depending on the parameters used [42].

Peak integrations in ^{1}H NMR spectra of the acid-digested materials (Figure S6) yield linker:modulator molar ratios of 1.0, 0.97, and 0.99 for Zr-UiO-66, Hf-UiO-66, and Zr-Hf-Zr-Hf-UiO-66, respectively, which are in excellent agreement with the presence of benzoate modulators in vacant sites from 4 missing BDC linkers per node. Missing-linker defects in UiO-66 are desirable because they allow access to coordination sites on the metal nodes for catalysis [43] or drug delivery, [44] but they may also compromise the thermal stability of the material [45].

Bright field TEM images of Zr-UiO-66, Hf-UiO-66, Zr-Hf-Zr-Hf-UiO-66 (Fig. 3) and Zr-Hf-UiO-66 (Figure S2) are consistent with the typical octahedral morphology of UiO-66, [37] with the triangular {1 1 1} facets appearing well defined. No evidence of large defects between Zr and Hf layers or impurity phases was observed. In Zr-Hf-UiO-66 and Zr-Hf-Zr-Hf-UiO-66, clear mass-thickness contrast corresponding to alternating layers of Zr and Hf-rich regions was observed. Because a constant amount of precursor material was added to the synthesis with each spike experiment, the layer thickness is expected to decrease with each added layer as the particle size (and thus outer surface area) increases. This prediction is consistent with the very thin and often difficult to identify outer Hf layer in particles of Zr-Hf-Zr-Hf-UiO-66. However, all particles observed in TEM images of the Zr-Hf-Zr-Hf-UiO-66 sample exhibited mass-thickness contrast accordant with the presence of at least two layers of material around the Zr-UiO-66 core. This indicates the lack of Zr-only or Hf-only particles or core–shell particles with fewer layers.

STEM-EDS data of representative Zr-Hf-UiO-66 (Figure S7) and Zr-

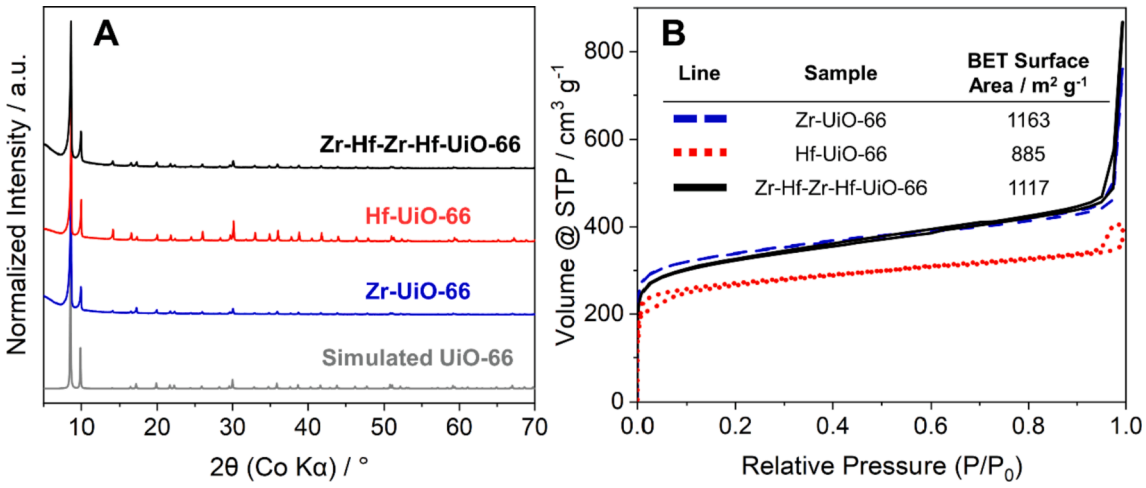

Fig. 2. Powder XRD patterns using Co Kα radiation (A) and N_2 sorption isotherms at 77 K (B) of Zr-UiO-66, Hf-UiO-66, and onion-like Zr-Hf-Zr-Hf-UiO-66. Surface areas in (B) were calculated using multi-point BET plots with relative pressure ranges of 0.05–0.20 (Zr-UiO-66 and Zr-Hf-Zr-Hf-UiO-66 and 0.05–0.25 (Hf-UiO-66).

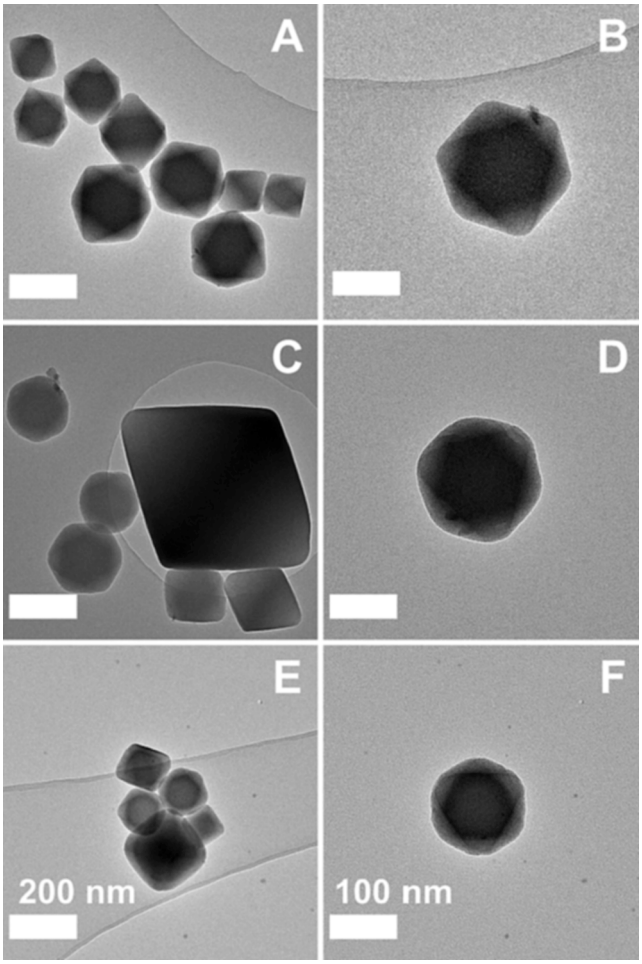

Fig. 3. Bright-field TEM images of Zr-UiO-66 (A–B), Hf-UiO-66 (C–D), and onion-like Zr-Hf-Zr-Hf-UiO-66 (E–F). Scale bars represent 200 nm (A, C, E) and 100 nm (B, D, F).

Hf-Zr-Hf-UiO-66 (Fig. 4) particles also demonstrate the presence of discrete Zr and Hf layers. Rings of alternating increases in Zr and Hf signals in the elemental maps correlate with areas of mass-thickness and Z-contrast observed in bright-field TEM and HAADF-STEM images, respectively. The outer Hf layer, which was often too thin to be resolved

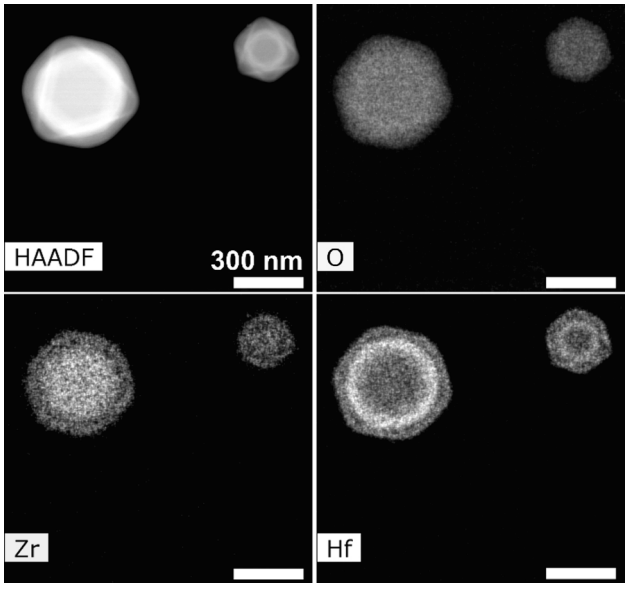

Fig. 4. High-angle annular dark field (HAADF) image and EDS elemental maps of onion-like Zr-Hf-Zr-Hf-UiO-66. Scale bars represent 300 nm.

in HAADF or bright-field images, is visible in Hf EDS maps. The oxygen EDS map shows no evidence of variation in oxygen content across the particle diameter.

The average Zr:Hf molar ratio in the Zr-Hf-Zr-Hf-UiO-66 nanoparticles was 1.3 ± 0.2 (as measured by EDS spectra of individual particles, $N = 12$), 1.4 ± 0.4 (based on approximating layers as spherical shells and thickness measurements from HAADF images, $N = 12$), and 1.29 ± 0.06 (as measured using ICP-OES analysis of a digestion solution of the materials). All three values are in good agreement, and the relatively small standard deviations suggest that the Zr:Hf ratio does not vary significantly between particles. All three experimental Zr:Hf ratios of ca. 1.3 are higher than the theoretical ratio of 1.0 predicted using the equimolar amounts of Zr and Hf precursors added in the seed synthesis and subsequent alternating spikes. This indicates lower yields from spikes of Hf material, which was consistent with the observed yields of Hf-UiO-66 (74 %), Zr-Hf-UiO-66 (49 %), and Zr-Hf-Zr-Hf-UiO-66 (75 %) as compared to Zr-UiO-66 (115 %). The greater than 100 % experimental yield of Zr-UiO-66 is likely because of residual solvent in the pores of the MOF. Slower growth rates of Hf nodes onto seed particles

could cause the lower yields of Hf-containing material. Increasing the reaction time may permit the growth of more Hf-UiO-66, which would shift the Zr:Hf ratio closer to unity.

Size distributions (Fig. 5) were measured after the initial syntheses of the seed crystals and after each spike of nodes and linker. The initial synthesis of Zr-UiO-66 seeds yielded a unimodal size distribution (Fig. 5A) with an average size of 110 ± 40 nm. The average size increased monotonically over 3 identical spikes of Zr-based nodes, while the standard deviation did not change appreciably. A similar trend was observed for Zr-Hf-Zr-Hf-UiO-66 (Fig. 5C), which initially had an average size of 80 ± 30 nm. These data are consistent with the deposition of new material onto existing particles rather than the nucleation of new crystals, which we would expect to result in an increasing standard deviation and a multimodal size distribution. Furthermore, the lack of Zr-only or Hf-only particles in TEM images of the Zr-Hf-Zr-Hf-UiO-66 sample supports the hypothesis that secondary nucleation did not occur. Even though the batch of Zr-Hf-Zr-Hf-UiO-66 contained the requisite starting material for the growth of individual Zr-UiO-66 and Hf-UiO-66 particles, the propensity for core–shell growth over nucleation was clear. On the other hand, the initial synthesis of Hf-UiO-66 seeds yielded a broad unimodal size distribution (Fig. 5B) with an average size of 400 ± 100 nm, roughly 4–5 times larger than Zr-UiO-66 and Zr-Hf-Zr-Hf-UiO-66. Large particle sizes and poor monodispersity of Hf-UiO-66 have also been reported by deKrafft *et al.*;[24] we hypothesize that the increased oxophilicity of Hf is a salient factor. With a Hf–O BDE ~ 5 % higher than that of Zr–O, [26] dissociation of the benzoate modulator from the Hf node to expose a vacant site for linker coordination is less favorable. Such a shift in equilibrium would slow nucleation and growth, leading to the formation of a few large particles rather than many small ones. The observed yields of Hf-containing UiO-66, which were lower than that of Zr-UiO-66, also suggest slower nucleation and growth of Hf-UiO-66. Secondary nucleation could explain the broader size distribution, as compared to the more monodisperse Zr-UiO-66 seeds, if nucleation of small Hf-UiO-66 particles continues as larger ones grow.

The first spike of metal nodes onto Hf-UiO-66 seed crystals produced a bimodal distribution of particle sizes with peaks centered around 100 nm and 550 nm. This means that new material was not consistently incorporated onto the initial seed particles. This phenomenon was reproducible over several identical syntheses but did not seem to negatively affect particle crystallinity or BET surface area. Ostwald ripening, whereby larger, more thermodynamically stable particles grow at the expense of smaller ones, could give rise to the observed bimodal size distribution in Hf-UiO-66. Liu *et al.* have controlled the extent of Ostwald ripening to deposit Zr-UiO-66 shells onto inorganic nanoparticles, [46] and it is reasonable to assume that similar ripening mechanisms are at play in the growth of Hf-UiO-66 in our work. Ongoing nucleation during the 48-h reaction period would also explain the emergence of a population of small particles while larger ones are still present. Interestingly, after the first spike, the general shape of the particle size distribution is consistent across subsequent spikes, with the two peaks simply moving to larger and larger sizes.

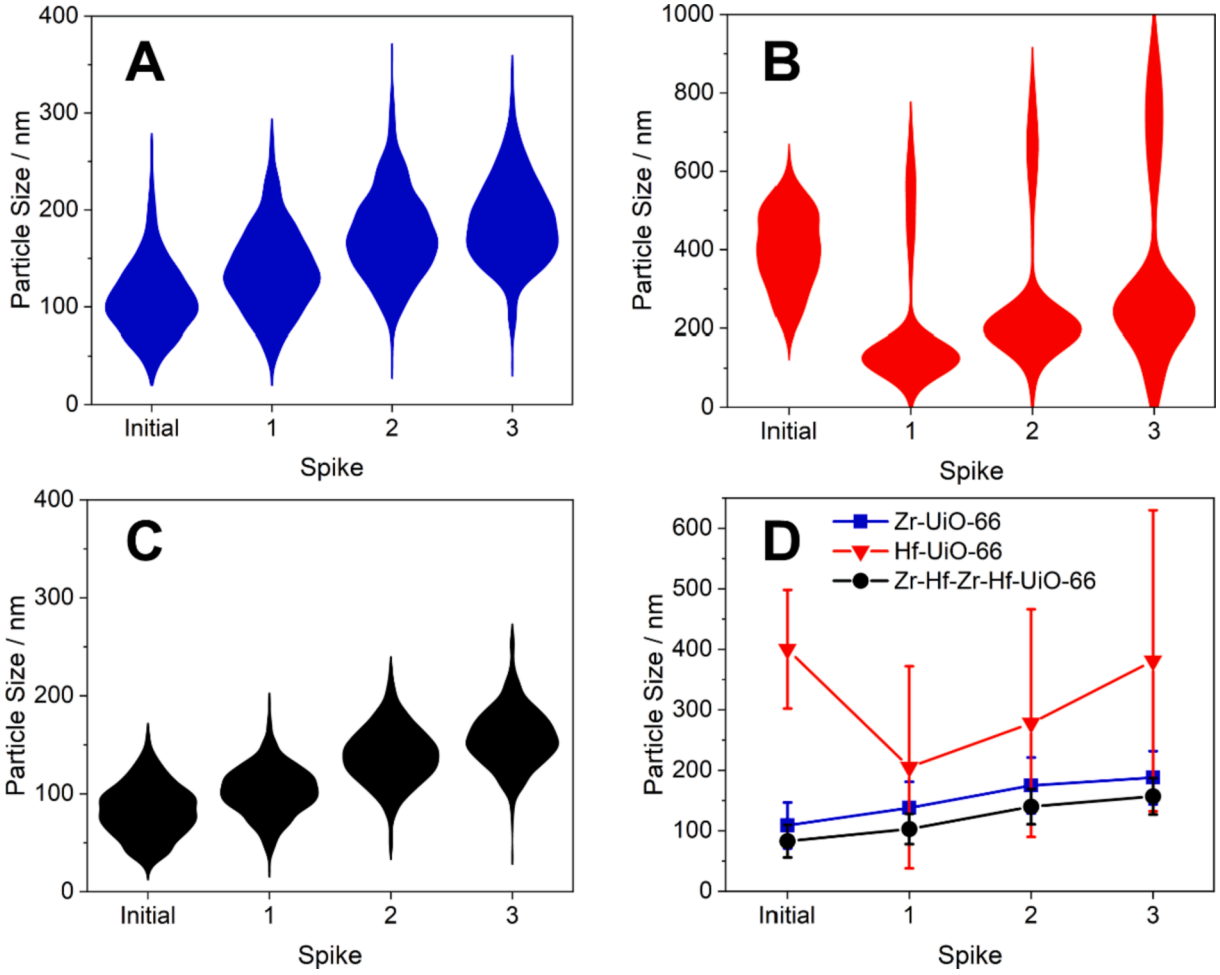

Fig. 5. Violin plots showing particle size distributions of Zr-UiO-66 (A), Hf-UiO-66 (B), and onion-like Zr-Hf-Zr-Hf-UiO-66 (C) and average sizes (D) after initial synthesis of seed particles and each spike of metal nodes and linker. Shape widths in (A–C) represent the relative number of measurements for each particle size, and error bars in (D) are ± 1 S.D. ($343 \leq N \leq 536$).

Ripening appears to be less important in the syntheses of Zr-UiO-66 and Zr-Hf-Zr-Hf-UiO-66, as neither exhibit bimodal size distributions after adding spikes of starting material and both exhibit particle size distributions with similar shapes after each subsequent spike. Moreover, the addition of Hf-based nodes to the suspension containing the Zr-UiO-66 seeds does not cause the same change in particle size distribution as observed with the spike of Hf-based nodes onto the Hf-UiO-66 seeds. This is consistent with the growth on the Zr-UiO-66 seeds being favored over nucleation of new Hf-UiO-66 particles. Because the crystal growth of Zr-Hf-Zr-Hf-UiO-66 was more like that of Zr-UiO-66 than Hf-UiO-66, we propose that the size distribution of seed particles and the identity of the core MOF are key factors in the growth of the onion-like material. It follows that control over particle size of onion-like UiO-66 with cores of Hf material may be substantially more difficult.

To characterize the onion-like particles from the perspective of their potential to serve as scaffolds for reactive sites, product materials were infiltrated with methanolic solutions of $Ni(OAc)_2{\cdot}4H_2O$. The nickel-loaded materials, which were designated Ni@Zr-UiO-66, Ni@Hf-UiO-66, Ni@Zr-Hf-UiO-66, and Ni@Zr-Hf-Zr-Hf-UiO-66, were successfully prepared with little to no loss of crystallinity, as characterized using XRD (Figure S4). Nickel was observed throughout the particles in EDS elemental maps (Fig. 6), but the average loading of 1.7 Ni atoms per node in Ni@Hf-UiO-66 is substantially higher than the value of 1.1 Ni atoms per node in Ni@Zr-UiO-66 (Table 1). Higher Ni^{2+} occupancies have been reported in nickel-loaded Hf-NU-1000 than Zr-NU-1000 (NU-1000 has the same nodes as UiO-66), and the bonding motifs of Ni^{2+} cations coordinated to the oxygen atoms of the nodes are known to differ between the two materials [38]. Though comparisons of solvothermal deposition of metal cations into Zr-UiO-66 and Hf-UiO-66 have not been discussed in the literature, our results align with the higher Brønsted acidity of Hf-UiO-66. That is, a higher population of deprotonated oxygen atoms in Hf-UiO-66 may accept more Ni^{2+} cations per node than in Zr-UiO-66.

Average Ni^{2+} occupancy in Ni@Zr-Hf-Zr-Hf-UiO-66 is intermediate (~1.3 Ni atoms per node) between Ni@Zr-UiO-66 and Ni@Hf-UiO-66, which is consistent with the presence of Ni in both Zr and Hf regions in STEM-EDS maps. We hypothesized that the Ni^{2+} to node ratios in Zr-rich and Hf-rich layers in Ni@Zr-Hf-Zr-Hf-UiO-66 would follow the trend seen in the measurements for Ni@Zr-UiO-66 and Ni@Hf-UiO-66, respectively, with distinct bands of Ni-rich regions in the Hf layers predicted. Variations in Ni^{2+} content are not discernable in the EDS maps of Ni@Zr-Hf-Zr-Hf-UiO-66 particles. However, spectra generated from different regions of the STEM-EDS maps (Figure S8) enabled quantitation of Ni^{2+} loading in each layer of the particles. In both Ni@Zr-Hf-UiO-66 and Ni@Zr-Hf-Zr-Hf-UiO-66, a significant difference between the $Ni:M_6$ ratios, where M_6 is the sum of Zr_6 and Hf_6 nodes, in the Zr-rich versus Hf-rich layers is discernable, with higher $Ni:M_6$ ratios observed for the Zr-rich regions as compared to the Hf-rich regions of the particles (Table S1). This apparent reversal of affinity of Ni^{2+} for Zr-UiO-66 as compared to Hf-UiO-66 is surprising. One possible explanation is the leaching of Ni^{2+} from the outermost layers during the washing steps, leaving more Ni^{2+} in the Zr-rich core. Indeed, a similar analysis of Ni@Zr-UiO-66 and Ni@Hf-UiO-66 reveals that $Ni:M_6$ ratios are lower near the edges of the particle as compared to the center (Figure S8 and Table S2). In Ni@Zr-UiO-66 and Ni@Hf-UiO-66, respectively, the $Ni:M_6$ ratios are ~ 30 % and ~ 10 % lower at the particle edges than near the middle. These findings suggest that the variation in Ni^{2+} content across the onion-like particles could simply be an effect of washing post-deposition, though the more Brønsted acidic Hf-UiO-66 seems to retain more Ni^{2+} than Zr-UiO-66 upon washing. Despite this unanticipated result, our work does demonstrate that transition metal ions or complexes may be post-synthetically installed into UiO-66 nanoparticles with distinct layers of Zr-rich and Hf-rich material. Differences in metal cation reactivity in such materials, or perhaps even those containing mixtures of Zr-based and Hf-based nodes or nodes containing both metal cations, could offer a unique route to controlling catalysis and chemical sensing.

Previous work on facet-dependent growth [34,47,48] and reactivity [49,50] of MOFs invites additional investigation of the location and behavior of active sites. While octahedral UiO-66 particles have cubic symmetry and eight crystallographically identical facets, using sequential spikes of different metal precursors as outlined in this work could differentiate the reactivities of distinct crystal facets in systems with lower symmetry. Good candidates for sequential spike crystal growth experiments include MOFs with hexagonal symmetry like NU-1000, which has been prepared with Zr, [10] Hf, [51] and Ce-based [52] nodes, and MIL-68, whose Al, [53] Ga, In, [54] Fe, [55] and V [56] analogues have been reported. By measuring the location and extent of the growth on seed crystals, additional morphological information may be accessed beyond gross estimates using XRD or other methods. Such

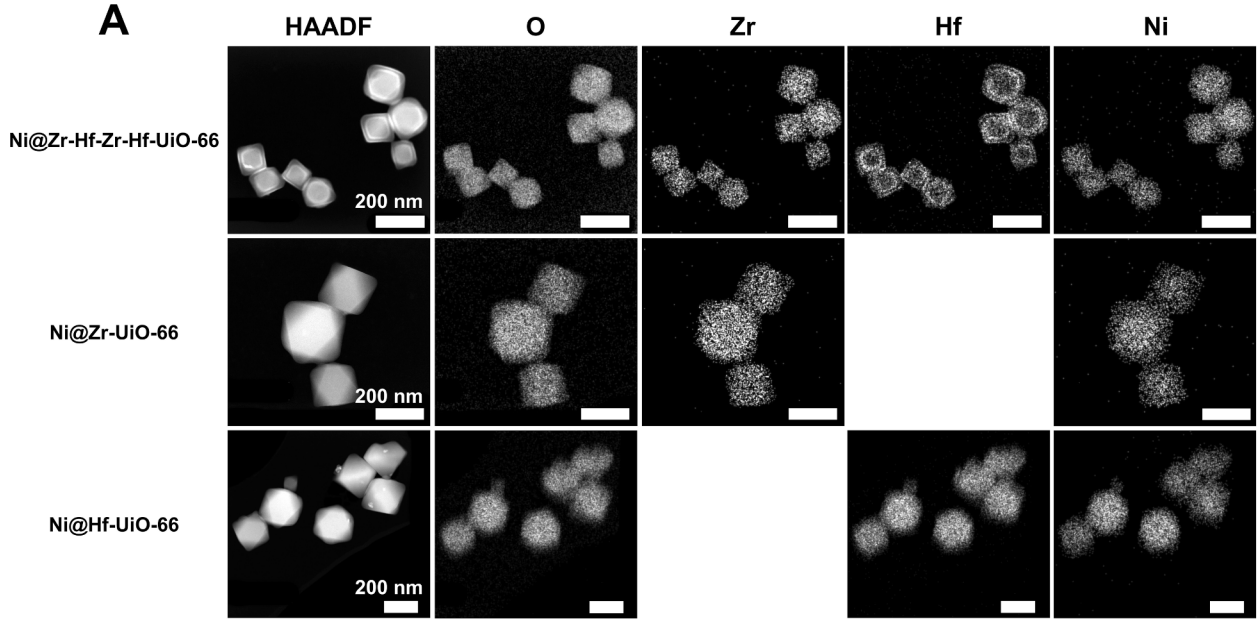

Fig. 6. High-angle annular dark field (HAADF) images and EDS elemental maps of nickel-loaded Zr-UiO-66, Hf-UiO-66, and onion-like Zr-Hf-Zr-Hf-UiO-66. Scale bars represent 200 nm.

Table 1
Nickel to metal node (M_6) ratios in nickel-loaded Zr-UiO-66, Hf-UiO-66, and onion-like Zr-Hf-Zr-Hf-UiO-66, as measured by EDS spectra and ICP-OES. Uncertainties are ± 1 S.D. (N = 10–12 particles for EDS).

Sample	Ni:M_6	
	EDS	ICP-OES
Ni@Zr-Hf-Zr-Hf-UiO-66	1.3 ± 0.2	1.4 ± 0.2
Ni@Zr-UiO-66	1.1 ± 0.2	1.1 ± 0.3
Ni@Hf-UiO-66	1.7 ± 0.5	1.7 ± 0.4

information is indispensable in the study of non-classical phenomena like oriented attachment/aggregation growth. Results could also inform computational models on anisotropic crystal growth. Finally, the range of metal cations used to construct MOFs in the literature allows this technique to be generalized to numerous systems.

4. Conclusion

Sequential spikes of starting material were used to synthesize crystalline, phase-pure nanoparticles of Zr-Hf-Zr-Hf-UiO-66 with an onion-like microstructure. Discrete regions of Zr and Hf nodes are apparent *via* mass-thickness contrast in bright-field TEM and Z-contrast in HAADF-STEM. Particles of Zr-Hf-Zr-Hf-UiO-66 contain ~ 30 % more Zr than Hf despite equimolar inputs of Zr and Hf starting material, which is likely a consequence of faster growth of the Zr-containing material. Particle size distributions, TEM images, and STEM-EDS elemental maps support our hypothesis that material from each spike was incorporated onto existing seed crystals instead of nucleating as new ones. Ni^{2+} cations were successfully installed into the materials, and Ni^{2+} loading was characterized using STEM-EDS, giving increasing Ni^{2+}:node ratios in the order Zr-UiO-66 < Zr-Hf-Zr-Hf-UiO-66 < Hf-UiO-66. Alternating layers of Zr and Hf-rich regions in Zr-Hf-Zr-Hf-UiO-66 were a simple aid in the visualization of crystal growth of individual MOF particles. This procedure may easily be extended to other MOFs to investigate reactive sites and facet-dependent growth mechanisms.

CRediT authorship contribution statement

Adam F. Cahn: Conceptualization, Methodology, Investigation, Validation, Formal analysis, Writing – original draft, Writing – review & editing, Visualization. **Rebecca L. Combs:** Conceptualization, Methodology, Investigation, Visualization, Validation, Formal analysis, Supervision, Writing – review & editing. **Ellen M. Monzo:** Investigation, Formal analysis, Supervision, Writing – review & editing. **Steven D. Prinslow:** Investigation, Formal analysis, Writing – review & editing. **Celina M. Harris:** Investigation, Formal analysis, Writing – review & editing. **R. Lee Penn:** Writing – review & editing, Methodology, Visualization, Formal analysis, Supervision, Project administration, Data curation, Funding acquisition.

Declaration of Competing Interest

The authors declare that they have no known competing financial interests or personal relationships that could have appeared to influence the work reported in this paper.

Data availability

Data will be made available on request.

Acknowledgment

This work was supported as part of the Inorganometallic Catalyst Design Center, an Energy Frontier Resource Center funded by the U.S. Department of Energy (DOE), Office of Science, Basic Energy Sciences (BES), under award DE-SC0012702. Parts of this work were carried out in the Characterization Facility, University of Minnesota, which receives partial support from the NSF through the MRSEC (Award Number DMR-2011401) and the NNCI (Award Number ECCS-2025124) programs. Research reported in this publication was supported by the Office of the Vice President of Research, College of Science and Engineering, and the Department of Chemistry at the University of Minnesota.

Appendix A. Supplementary material

Supplementary data to this article can be found online at https://doi.org/10.1016/j.jcrysgro.2022.126911.

References

[1] A. Muñoz, P. Leo, G. Orcajo, F. Martínez, G. Calleja, URJC-1-MOF as New Heterogeneous Recyclable Catalyst for C-Heteroatom Coupling Reactions, ChemCatChem 11 (2019) 3376–3380, https://doi.org/10.1002/cctc.201900906.
[2] M. Bonneau, C. Lavenn, P. Ginet, K. Otake, S. Kitagawa, Upscale Synthesis of a Binary Pillared Layered MOF for Hydrocarbon Gas Storage and Separation, Green Chem. 22 (2020) 718–724, https://doi.org/10.1039/C9GC03561C.
[3] K. Müller-Buschbaum, F. Beuerle, C. Feldmann, MOF Based Luminescence Tuning and Chemical/Physical Sensing, Microporous Mesoporous Mater. 216 (2015) 171–199, https://doi.org/10.1016/j.micromeso.2015.03.036.
[4] V. Stavila, A.A. Talin, M.D. Allendorf, MOF-Based Electronic and Opto-Electronic Devices, Chem. Soc. Rev. 43 (2014) 5994–6010, https://doi.org/10.1039/C4CS00096J.
[5] C. Lin, B. Chi, C. Xu, C. Zhang, F. Tian, Z. Xu, L. Li, A.K. Whittaker, J. Wang, Multifunctional Drug Carrier on the Basis of 3d–4f Fe/La-MOFs for Drug Delivery and Dual-Mode Imaging, J. Mater. Chem. B 7 (2019) 6612–6622, https://doi.org/10.1039/C9TB01509D.
[6] P. Kumar, K. Vellingiri, K.-H. Kim, R.J.C. Brown, M.J. Manos, Modern Progress in Metal-Organic Frameworks and Their Composites for Diverse Applications, Microporous Mesoporous Mater. 253 (2017) 251–265, https://doi.org/10.1016/j.micromeso.2017.07.003.
[7] T.E. Webber, S.P. Desai, R.L. Combs, S. Bingham, C.C. Lu, R.L. Penn, Size Control of the MOF NU-1000 through Manipulation of the Modulator/Linker Competition, Cryst. Growth Des. 20 (2020) 2965–2972, https://doi.org/10.1021/acs.cgd.9b01590.
[8] T.E. Webber, W.-G. Liu, S.P. Desai, C.C. Lu, D.G. Truhlar, R.L. Penn, Role of a Modulator in the Synthesis of Phase-Pure NU-1000, ACS Appl. Mater. Interfaces 9 (2017) 39342–39346, https://doi.org/10.1021/acsami.7b11348.
[9] P. Yang, F. Mao, Y. Li, Q. Zhuang, J. Gu, Hierarchical Porous Zr-Based MOFs Synthesized by a Facile Monocarboxylic Acid Etching Strategy, Chem. - Eur. J. 24 (2018) 2962–2970, https://doi.org/10.1002/chem.201705020.
[10] J.E. Mondloch, W. Bury, D. Fairen-Jimenez, S. Kwon, E.J. DeMarco, M.H. Weston, A.A. Sarjeant, S.T. Nguyen, P.C. Stair, R.Q. Snurr, O.K. Farha, J.T. Hupp, Vapor-Phase Metalation by Atomic Layer Deposition in a Metal-Organic Framework, J. Am. Chem. Soc. 135 (2013) 10294–10297, https://doi.org/10.1021/ja4050828.
[11] G. Zahn, P. Zerner, J. Lippke, F.L. Kempf, S. Lilienthal, C.A. Schröder, A. M. Schneider, P. Behrens, Insight into the Mechanism of Modulated Syntheses. In Situ Synchrotron Diffraction Studies on the Formation of Zr-Fumarate MOF, CrystEngComm 16 (2014) 9198–9207, https://doi.org/10.1039/C4CE01095G.
[12] P. Cubillas, M.W. Anderson, M.P. Attfield, Crystal Growth Mechanisms and Morphological Control of the Prototypical Metal-Organic Framework MOF-5 Revealed by Atomic Force Microscopy, Chem. - Eur. J. 18 (2012) 15406–15415, https://doi.org/10.1002/chem.201202261.
[13] J.P. Patterson, P. Abellan, M.S. Denny, C. Park, N.D. Browning, S.M. Cohen, J. E. Evans, N.C. Gianneschi, Observing the Growth of Metal-Organic Frameworks by in Situ Liquid Cell Transmission Electron Microscopy, J. Am. Chem. Soc. 137 (23) (2015) 7322–7328.
[14] J.H. Park, K.M. Choi, H.J. Jeon, Y.J. Choi, J.K. Kang, In-Situ Observation for Growth of Hierarchical Metal-Organic Frameworks and Their Self-Sequestering Mechanism for Gas Storage, Sci. Rep. 5 (2015) 12045, https://doi.org/10.1038/srep12045.
[15] V. Stavila, J. Volponi, A.M. Katzenmeyer, M.C. Dixon, M.D. Allendorf, Kinetics and Mechanism of Metal-Organic Framework Thin Film Growth: Systematic Investigation of HKUST-1 Deposition on QCM Electrodes, Chem. Sci. 3 (2012) 1531–1540, https://doi.org/10.1039/C2SC20065A.
[16] J. Cravillon, R. Nayuk, S. Springer, A. Feldhoff, K. Huber, M. Wiebcke, Controlling Zeolitic Imidazolate Framework Nano- and Microcrystal Formation: Insight into Crystal Growth by Time-Resolved In Situ Static Light Scattering, Chem. Mater. 23 (2011) 2130–2141, https://doi.org/10.1021/cm103571y.
[17] M. Haouas, C. Volkringer, T. Loiseau, G. Férey, F. Taulelle, In Situ NMR, Ex Situ XRD and SEM Study of the Hydrothermal Crystallization of Nanoporous Aluminum Trimesates MIL-96, MIL-100, and MIL-110, Chem. Mater. 24 (2012) 2462–2471, https://doi.org/10.1021/cm300439e.
[18] M.R. Armstrong, S. Senthilnathan, C.J. Balzer, B. Shan, L. Chen, B. Mu, Particle Size Studies to Reveal Crystallization Mechanisms of the Metal Organic Framework HKUST-1 during Sonochemical Synthesis, Ultrason. Sonochem. 34 (2017) 365–370, https://doi.org/10.1016/j.ultsonch.2016.06.011.

[19] S. Lee, S. Oh, M. Oh, Atypical Hybrid Metal-Organic Frameworks (MOFs): A Combinative Process for MOF-on-MOF Growth, Etching, and Structure Transformation, Angew. Chem. Int. Ed. 59 (2020) 1327–1333, https://doi.org/10.1002/anie.201912986.

[20] J.J. De Yoreo, P.U.P.A. Gilbert, N.A.J.M. Sommerdijk, R.L. Penn, S. Whitelam, D. Joester, H. Zhang, J.D. Rimer, A. Navrotsky, J.F. Banfield, A.F. Wallace, F. M. Michel, F.C. Meldrum, H. Cölfen, P.M. Dove, Crystallization by Particle Attachment in Synthetic Biogenic, and Geologic Environments, Science 349 (2015) aaa6760, https://doi.org/10.1126/science.aaa6760.

[21] N. Sikdar, M. Bhogra, U.V. Waghmare, T.K. Maji, Oriented Attachment Growth of Anisotropic Meso/Nanoscale MOFs: Tunable Surface Area and CO_2 Separation, J. Mater. Chem. A. 5 (2017) 20959–20968, https://doi.org/10.1039/C7TA02896B.

[22] G. Mouchaham, L. Cooper, N. Guillou, C. Martineau, E. Elkaïm, S. Bourrelly, P. L. Llewellyn, C. Allain, G. Clavier, C. Serre, T. Devic, A Robust Infinite Zirconium Phenolate Building Unit to Enhance the Chemical Stability of Zr MOFs, Angew. Chem. Int. Ed. 54 (2015) 13297–13301, https://doi.org/10.1002/anie.201507058.

[23] T. Devic, C. Serre, High Valence 3p and Transition Metal Based MOFs, Chem. Soc. Rev. 43 (2014) 6097–6115, https://doi.org/10.1039/C4CS00081A.

[24] K.E. deKrafft, W.S. Boyle, L.M. Burk, O.Z. Zhou, W. Lin, Zr- and Hf-Based Nanoscale Metal-Organic Frameworks as Contrast Agents for Computed Tomography, J. Mater. Chem. 22 (2012) 18139, https://doi.org/10.1039/c2jm32299d.

[25] Z. Hu, A. Nalaparaju, Y. Peng, J. Jiang, D. Zhao, Modulated Hydrothermal Synthesis of UiO-66(Hf)-Type Metal-Organic Frameworks for Optimal Carbon Dioxide Separation, Inorg. Chem. 55 (2016) 1134–1141, https://doi.org/10.1021/acs.inorgchem.5b02312.

[26] V.R. Bakuru, S.R. Churipard, S.P. Maradur, S.B. Kalidindi, Exploring the Brønsted Acidity of UiO-66 (Zr, Ce, Hf) Metal-Organic Frameworks for Efficient Solketal Synthesis from Glycerol Acetalization, Dalton Trans. 48 (2019) 843–847, https://doi.org/10.1039/C8DT03512A.

[27] W. Morris, S. Wang, D. Cho, E. Auyeung, P. Li, O.K. Farha, C.A. Mirkin, Role of Modulators in Controlling the Colloidal Stability and Polydispersity of the UiO-66 Metal-Organic Framework, ACS Appl. Mater. Interfaces 9 (2017) 33413–33418, https://doi.org/10.1021/acsami.7b01040.

[28] S.-X. Lin, W.-L. Pan, R.-J. Niu, Y. Liu, J.-X. Chen, W.-H. Zhang, J.-P. Lang, D. J. Young, Effective Loading of Cisplatin Into a Nanoscale UiO-66 Metal-Organic Framework With Preformed Defects, Dalton Trans. 48 (2019) 5308–5314, https://doi.org/10.1039/C9DT00719A.

[29] J.F. Blandez, A. Santiago-Portillo, S. Navalón, M. Giménez-Marqués, M. Álvaro, P. Horcajada, H. García, Influence of Functionalization of Terephthalate Linker on the Catalytic Activity of UiO-66 for Epoxide Ring Opening, J. Mol. Catal. A: Chem. 425 (2016) 332–339, https://doi.org/10.1016/j.molcata.2016.10.022.

[30] P. Wu, Q. Du, L. Chen, M. Yang, Y. Sun, H. Zhi, P. Dramou, H. He, Fluorescence Determination of Quercetin in Food Samples Using Polyhedron-Shaped MOF@MOF(NUZ-8) Based on NH_2-UiO-66 and ZIF-8, Microchim. Acta 188 (2021) 29, https://doi.org/10.1007/s00604-020-04664-2.

[31] J. Ren, N.M. Musyoka, H.W. Langmi, B.C. North, M. Mathe, X. Kang, Fabrication of Core-Shell MIL-101(Cr)@UiO-66(Zr) Nanocrystals for Hydrogen Storage, Int. J. Hydrog. Energy 39 (2014) 14912–14917, https://doi.org/10.1016/j.ijhydene.2014.07.056.

[32] J. Ha, H.R. Moon, Synthesis of MOF-on-MOF Architectures in the Context of Interfacial Lattice Matching, CrystEngComm 23 (2021) 2337–2354, https://doi.org/10.1039/D0CE01883J.

[33] J. Son, H.J. Lee, M. Oh, Systematic Formation of Multilayered Core-Shell Microspheres through the Multistep Growth of Coordination Polymers, Chem. - Eur. J. 19 (2013) 6546–6550, https://doi.org/10.1002/chem.201300585.

[34] H.J. Lee, Y.J. Cho, W. Cho, M. Oh, Controlled Isotropic or Anisotropic Nanoscale Growth of Coordination Polymers: Formation of Hybrid Coordination Polymer Particles, ACS Nano 7 (2013) 491–499, https://doi.org/10.1021/nn304597h.

[35] K. Koh, A.G. Wong-Foy, A.J. Matzger, MOF@MOF: Microporous Core-Shell Architectures, Chem. Commun. 41 (2009) 6162–6164, https://doi.org/10.1039/b904526k.

[36] T.-Y. Luo, C. Liu, X.Y. Gan, P.F. Muldoon, N.A. Diemler, J.E. Millstone, N.L. Rosi, Multivariate Stratified Metal-Organic Frameworks: Diversification Using Domain Building Blocks, J. Am. Chem. Soc. 141 (2019) 2161–2168, https://doi.org/10.1021/jacs.8b13502.

[37] A. Schaate, P. Roy, A. Godt, J. Lippke, F. Waltz, M. Wiebcke, P. Behrens, Modulated Synthesis of Zr-Based Metal-Organic Frameworks: From Nano to Single Crystals, Chem. - Eur. J. 17 (2011) 6643–6651, https://doi.org/10.1002/chem.201003211.

[38] X. Wang, X. Zhang, R. Pandharkar, J. Lyu, D. Ray, Y. Yang, S. Kato, J. Liu, M. C. Wasson, T. Islamoglu, Z. Li, J.T. Hupp, C.J. Cramer, L. Gagliardi, O.K. Farha, Insights into the Structure-Activity Relationships in Metal-Organic Framework-Supported Nickel Catalysts for Ethylene Hydrogenation, ACS Catal. 10 (2020) 8995–9005, https://doi.org/10.1021/acscatal.0c01844.

[39] J.H. Cavka, S. Jakobsen, U. Olsbye, N. Guillou, C. Lamberti, S. Bordiga, K. P. Lillerud, A New Zirconium Inorganic Building Brick Forming Metal Organic Frameworks with Exceptional Stability, J. Am. Chem. Soc. 130 (2008) 13850–13851, https://doi.org/10.1021/ja8057953.

[40] S. Diring, S. Furukawa, Y. Takashima, T. Tsuruoka, S. Kitagawa, Controlled Multiscale Synthesis of Porous Coordination Polymer in Nano/Micro Regimes, Chem. Mater. 22 (2010) 4531–4538, https://doi.org/10.1021/cm101778g.

[41] M.J. Katz, Z.J. Brown, Y.J. Colón, P.W. Siu, K.A. Scheidt, R.Q. Snurr, J.T. Hupp, O. K. Farha, A Facile Synthesis of UiO-66, UiO-67 and Their Derivatives, Chem. Commun. 49 (2013) 9449–9451, https://doi.org/10.1039/C3CC46105J.

[42] J.W.M. Osterrieth, J. Rampersad, D. Madden, N. Rampal, L. Skoric, B. Connolly, M. D. Allendorf, V. Stavila, J.L. Snider, R. Ameloot, J. Marreiros, C. Ania, D. Azevedo, E. Vilarrasa-Garcia, B.F. Santos, X.-H. Bu, Z.e. Chang, H. Bunzen, N.R. Champness, S.L. Griffin, B. Chen, R.-B. Lin, B. Coasne, S. Cohen, J.C. Moreton, Y.J. Colón, L. Chen, R. Clowes, F.-X. Coudert, Y. Cui, B. Hou, D.M. D'Alessandro, P.W. Doheny, M. Dincă, C. Sun, C. Doonan, M.T. Huxley, J.D. Evans, P. Falcaro, R. Ricco, O. Farha, K.B. Idrees, T. Islamoglu, P. Feng, H. Yang, R.S. Forgan, D. Bara, S. Furukawa, E. Sanchez, J. Gascon, S. Telalović, S.K. Ghosh, S. Mukherjee, M. R. Hill, M.M. Sadiq, P. Horcajada, P. Salcedo-Abraira, K. Kaneko, R. Kukobat, J. Kenvin, S. Keskin, S. Kitagawa, K.-I. Otake, R.P. Lively, S.J.A. DeWitt, P. Llewellyn, B.V. Lotsch, S.T. Emmerling, A.M. Pütz, C. Martí-Gastaldo, N. M. Padial, J. García-Martínez, N. Linares, D. Maspoch, J.A. Suárez del Pino, P. Moghadam, R. Oktavian, R.E. Morris, P.S. Wheatley, J. Navarro, C. Petit, D. Danaci, M.J. Rosseinsky, A.P. Katsoulidis, M. Schröder, X. Han, S. Yang, C. Serre, G. Mouchaham, D.S. Sholl, R. Thyagarajan, D. Siderius, R.Q. Snurr, R. B. Goncalves, S. Telfer, S.J. Lee, V.P. Ting, J.L. Rowlandson, T. Uemura, T. Iiyuka, M.A. van der Veen, D. Rega, V. Van Speybroeck, S.M.J. Rogge, A. Lamaire, K. S. Walton, L.W. Bingel, S. Wuttke, J. Andreo, O. Yaghi, B. Zhang, C.T. Yavuz, T. S. Nguyen, F. Zamora, C. Montoro, H. Zhou, A. Kirchon, D. Fairen-Jimenez, How Reproducible are Surface Areas Calculated from the BET Equation? Adv. Mater. 34 (27) (2022) 2201502.

[43] X. Chen, Y. Lyu, Z. Wang, X. Qiao, B.C. Gates, D. Yang, Tuning $Zr_{12}O_{22}$ Node Defects as Catalytic Sites in the Metal-Organic Framework hcp UiO-66, ACS Catal. 10 (2020) 2906–2914, https://doi.org/10.1021/acscatal.9b04905.

[44] I. Abánades Lázaro, C.J.R. Wells, R.S. Forgan, Multivariate Modulation of the Zr MOF UiO-66 for Defect-Controlled Combination Anticancer Drug Delivery, Angew. Chem. Int. Ed. 59 (2020) 5211–5217, https://doi.org/10.1002/anie.201915848.

[45] G.C. Shearer, S. Chavan, J. Ethiraj, J.G. Vitillo, S. Svelle, U. Olsbye, C. Lamberti, S. Bordiga, K.P. Lillerud, Tuned to Perfection: Ironing Out the Defects in Metal-Organic Framework UiO-66, Chem. Mater. 26 (2014) 4068–4071, https://doi.org/10.1021/cm501859p.

[46] Y. Liu, Y. Yang, Y. Sun, J. Song, N.G. Rudawski, X. Chen, W. Tan, Ostwald Ripening-Mediated Grafting of Metal-Organic Frameworks on a Single Colloidal Nanocrystal to Form Uniform and Controllable MXF, J. Am. Chem. Soc. 141 (2019) 7407–7413, https://doi.org/10.1021/jacs.9b01563.

[47] X.-Y. Liu, W.-S. Lo, C. Wu, B.P. Williams, L. Luo, Y. Li, L.-Y. Chou, Y. Lee, C.-K. Tsung, Tuning Metal-Organic Framework Nanocrystal Shape through Facet-Dependent Coordination, Nano Lett. 20 (2020) 1774–1780, https://doi.org/10.1021/acs.nanolett.9b04997.

[48] S. Choi, T. Kim, H. Ji, H.J. Lee, M. Oh, Isotropic and Anisotropic Growth of Metal-Organic Framework (MOF) on MOF: Logical Inference on MOF Structure Based on Growth Behavior and Morphological Feature, J. Am. Chem. Soc. 138 (2016) 14434–14440, https://doi.org/10.1021/jacs.6b08821.

[49] L. Chen, B. Duan, Q. Luo, Z. Gu, J. Liu, C. Duan, Facet-Dependent Catalytic Activity of ZIF-8 Nanocubes and Rhombic Dodecahedra Based on Tracing Substrate Diffusion in Pores by SERS: A Case Study for Surface Catalysis of MOFs, Catal. Sci. Technol. 6 (2016) 1616–1620, https://doi.org/10.1039/C5CY01882J.

[50] L.-Y. Pang, P. Wang, J.-J. Gao, Y. Wen, H. Liu, An Active Metal-Organic Anion Framework with Highly Exposed SO_4^{2-} on 001 Facets for the Enhanced Electrochemical Detection of Trace Fe3+, J. *Electroanal. Chem.* 836 (2019) 85–93, https://doi.org/10.1016/j.jelechem.2019.01.067.

[51] H. Beyzavi, R.C. Klet, S. Tussupbayev, J. Borycz, N.A. Vermeulen, C.J. Cramer, J. F. Stoddart, J.T. Hupp, O.K. Farha, A Hafnium-Based Metal-Organic Framework as an Efficient and Multifunctional Catalyst for Facile CO_2 Fixation and Regioselective and Enantioretentive Epoxide Activation, J. Am. Chem. Soc. 136 (2014) 15861–15864, https://doi.org/10.1021/ja508626n.

[52] S. Smolders, A. Struyf, H. Reinsch, B. Bueken, T. Rhauderwiek, L. Mintrop, P. Kurz, N. Stock, D.E. De Vos, A Precursor Method for the Synthesis of New Ce(IV) MOFs with Reactive Tetracarboxylate Linkers, Chem. Commun. 54 (2018) 876–879, https://doi.org/10.1039/C7CC08200B.

[53] Z. Wang, M. Babucci, Y. Zhang, Y. Wen, L. Peng, B. Yang, B.C. Gates, D. Yang, Dialing in Catalytic Sites on Metal Organic Framework Nodes: MIL-53(Al) and MIL-68(Al) Probed with Methanol Dehydration Catalysis, ACS Appl. Mater. Interfaces 12 (2020) 53537–53546, https://doi.org/10.1021/acsami.0c16559.

[54] C. Volkringer, M. Meddouri, T. Loiseau, N. Guillou, J. Marrot, G. Férey, M. Haouas, F. Taulelle, N. Audebrand, M. Latroche, The Kagomé Topology of the Gallium and Indium Metal-Organic Framework Types with a MIL-68 Structure: Synthesis, XRD, Solid-State NMR Characterizations, and Hydrogen Adsorption, Inorg. Chem. 47 (2008) 11892–11901, https://doi.org/10.1021/ic801624v.

[55] A. Fateeva, P. Horcajada, T. Devic, C. Serre, J. Marrot, J. Grenèche, M. Morcrette, J. Tarascon, G. Maurin, G. Férey, Synthesis, Structure, Characterization, and Redox Properties of the Porous MIL-68(Fe) Solid, Eur. J. Inorg. Chem. 2010 (2010) 3789–3794, https://doi.org/10.1002/ejic.201000486.

[56] K. Barthelet, J. Marrot, G. Férey, D. Riou, V III (OH){O_2C–C_6H_4–CO_2}.(HO_2C–C_6H_4–$CO_2H)_x(DMF)_y(H_2O)_z$ (or MIL-68), a new vanadocarboxylate with a large pore hybrid topology : reticular synthesis with infinite inorganic building blocks? Chem. Commun. (5) (2004) 520–521.